

Accurate and Complete Surface Reconstruction from 3D Gaussians via Direct SDF Learning

Wenzhi Guo, Guangchi Fang, Mingqing Wei, Jie Qin, Bing Wang*

Abstract—3D Gaussian Splatting (3DGS) has recently emerged as a powerful paradigm for photorealistic view synthesis, representing scenes with spatially distributed Gaussian primitives. While highly effective for rendering, achieving accurate and complete surface reconstruction remains challenging due to the unstructured nature of the representation and the absence of explicit geometric supervision. In this work, we propose DiGS, a unified framework that embeds Signed Distance Field (SDF) learning directly into the 3DGS pipeline, thereby enforcing strong and interpretable surface priors. By associating each Gaussian with a learnable SDF value, DiGS explicitly aligns primitives with underlying geometry and improves cross-view consistency. To further ensure dense and coherent coverage, we design a geometry-guided grid growth strategy that adaptively distributes Gaussians along geometry-consistent regions under a multi-scale hierarchy. Extensive experiments on standard benchmarks, including DTU, Mip-NeRF 360, and Tanks & Temples, demonstrate that DiGS consistently improves reconstruction accuracy and completeness while retaining high rendering fidelity. Our code is available at <https://github.com/DARYL-GWZ/DIGS>.

Index Terms—3D Gaussian Splatting, Surface reconstruction, Rendering.

I. INTRODUCTION

Recent advances in *3D Gaussian Splatting* (3DGS) [1] have transformed neural scene representation and rendering. By modeling a scene as a collection of anisotropic Gaussian primitives and rendering them through a carefully engineered rasterization pipeline, 3DGS achieves real-time, photo-realistic view synthesis. Its efficiency and fidelity have quickly spurred adoption in diverse applications, ranging from augmented and virtual reality [2]–[5] to autonomous driving [6]–[8].

Despite these advances, accurate geometry reconstruction remains a fundamental challenge for Gaussian-based representations. Unlike volumetric fields or mesh-based methods, Gaussian primitives are inherently unstructured and provide only weak geometric cues under multi-view supervision. As a result, they often exhibit drift and misalignment with underlying surfaces, leading to limited reconstruction fidelity [9]–[11]. Moreover, existing growth strategies for Gaussian models [1], [12] typically produce sparse and uneven distributions, failing

W. Guo is with the Department of Aeronautical and Aviation Engineering, The Hong Kong Polytechnic University, Hong Kong SAR, China and the Department of Computer Science and Technology, Nanjing University, Nanjing, China (e-mail: wenzhi.guo@connect.polyu.hk).

Mingqing Wei and Jie Qin are with School of Artificial Intelligence, Nanjing University of Aeronautics and Astronautics, Nanjing, China, and the (e-mail: mqwei@nuaa.edu.cn, jie.qin@nuaa.edu.cn).

Guangchi Fang and Bing Wang are with the Department of Aeronautical and Aviation Engineering, The Hong Kong Polytechnic University, Hong Kong SAR, China (e-mail: guangchi.fang@gmail.com, bingwang@polyu.edu.hk)

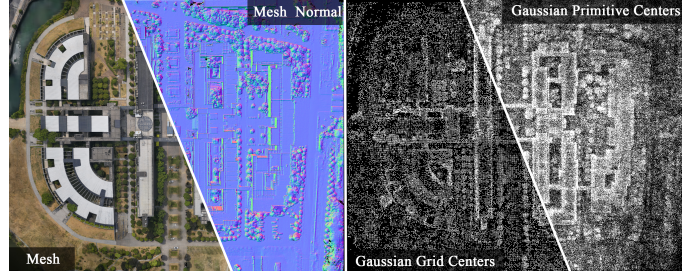


Fig. 1. **Conceptual Overview of DiGS.** DiGS advances Gaussian splatting from an appearance-driven representation toward a geometry-preserving paradigm, by embedding signed distance supervision into Gaussian primitives under a geometry-guided growth strategy.

to guarantee comprehensive scene coverage in complex or low-texture environments. These shortcomings suggest that current pipelines are largely appearance-driven, with geometry treated as an auxiliary objective rather than a core principle.

To address this, recent advances have sought to augment Gaussian splatting with stronger geometric priors. Geometric regularization methods [13], [14] introduce constraints such as normals or silhouettes, while surface extraction pipelines [12], [15] recover meshes only in a post-processing stage. SDF-based formulations provide a more direct coupling to geometry: 3DGSR [16] supervises Gaussians with signed distance values but suffers from artifacts under sparse guidance, and GSDF [17] adopts a dual-branch optimization that separates rendering and reconstruction, thereby increasing model complexity and weakening consistency between appearance and geometry. Similarly, PGSR [14] leverages composite geometric losses but requires post-training refinement for completeness, while Octree-GS [12] employs hierarchical multi-scale expansion guided primarily by appearance, often resulting in uneven coverage. Collectively, these approaches demonstrate the potential of SDF-augmented Gaussians, yet they leave unresolved the fundamental question of how geometry and appearance can be unified within a single, efficient framework. Collectively, these approaches demonstrate the potential of SDF-augmented Gaussians, yet they leave unresolved the fundamental question: how can geometry and appearance be unified within a single Gaussian framework, such that signed distance priors and growth strategies are jointly leveraged to achieve both accurate and complete surface reconstruction?

In this paper, we present **DiGS**, a unified framework that advances Gaussian splatting from an appearance-driven representation to a geometry-preserving paradigm. Unlike prior approaches that either impose weak geometric regularization

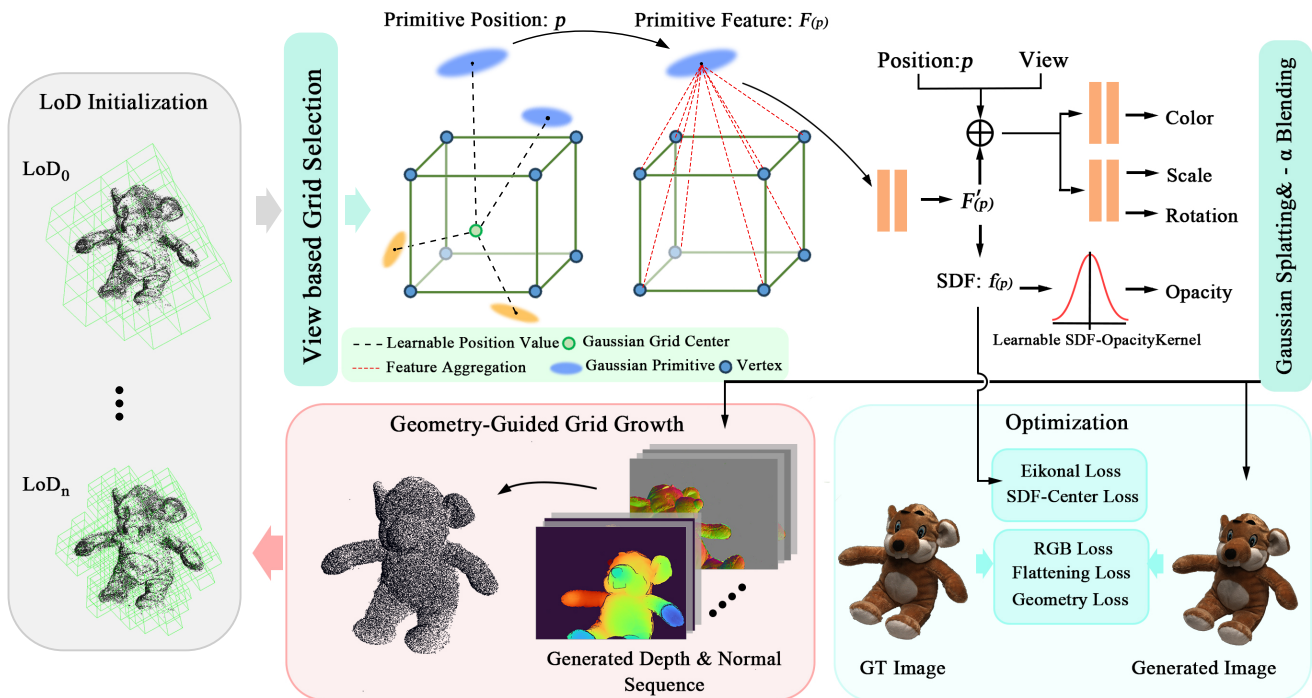


Fig. 2. **Detailed Framework of DiGS.** Starting from an SfM-initialized LoD grid, DiGS associates each cell with SDF-augmented Gaussians. Gaussian splatting and signed distance values are jointly predicted, with SDFs converted to opacity via a differentiable kernel. During training, a geometry-guided grid growth strategy expands Gaussians along geometry-consistent regions.

[14], [15] or decouple geometry and appearance into separate optimization branches [16], [17], DiGS integrates signed distance supervision directly into the Gaussian primitives, treating geometry as a first-class objective within the rendering pipeline. Each Gaussian is constrained by a learned signed distance value at its center, while a geometry-guided grid growth strategy systematically expands Gaussians along surface-consistent regions under a multi-scale level-of-detail (LoD) hierarchy. Crucially, SDF learning and geometry-guided grids growth are mutually dependent and jointly optimized: SDF supervision prevents Gaussian drift and grids growth guarantees surface completeness. Their tight coupling forms a necessary and self-reinforcing system, establishing DiGS as a new unified paradigm for geometry-aware Gaussian splatting that simultaneously achieves high-fidelity rendering and accurate surface reconstruction.

The main contributions are summarized as follows:

- We propose DiGS, a unified SDF-Gaussian framework, which directly embeds signed distance supervision into Gaussian primitives, achieving precise and consistent surface reconstruction.
- We develop a geometry-guided Gaussian grid growth mechanism that facilitates dense and spatially coherent coverage, particularly effective for complex or low-texture geometries.
- Extensive experiments on DTU, Mip-NeRF 360, and Tanks & Temples demonstrate consistent improvements in reconstruction accuracy and completeness compared to state-of-the-art Gaussian-based and hybrid methods.

II. RELATED WORK

A. Neural Surface Reconstruction

Neural surface reconstruction has evolved as a result of the interplay between implicit representations and geometric constraints. The pioneering work of NeRF [18] introduced volumetric rendering for view synthesis, but it faced significant limitations in surface modeling due to its density-based formulation, which lacked explicit geometric constraints. To address this, NeuS [19] and VolSDF [20] tightly coupled Signed Distance Fields (SDFs) with probabilistic volume rendering, enabling surface extraction through the zero-level set of the SDF, offering a more precise model for surface representation. These methods laid the foundation for surface-aware neural rendering but still struggled with handling complex geometries or large-scale scenes. A comprehensive survey of such neural implicit surface reconstruction paradigms is provided in [21], which systematizes recent advances and open challenges.

Subsequent works advanced the state of geometric fidelity through hybrid implicit-explicit representations. For example, UNISURF [22] unified implicit surfaces with volume rendering, offering improved detail preservation. Similarly, MonoSDF [23] and Geo-Neus [24] introduced monocular depth and normal priors for regularization, helping stabilize the optimization process by providing additional geometric priors. Extensions such as Vox-Surf [25] explored voxel-based implicit surface representation, while H-SDF [26] proposed a hybrid sign-distance formulation to support arbitrary topologies. Indoor scene reconstruction has also benefited from hybrid priors, as shown in [27], where fine-grained geometry is recovered by leveraging normal enhancements. In parallel,

semantic-driven surface modeling from point clouds, such as RangeUDF [28], demonstrated that semantic cues can further improve surface reconstruction robustness in challenging real-world environments.

Beyond hybrid priors, point-guided approaches such as PG-NeuS [29] and its progressive-growing tri-plane extension PGT-NeuS [30] improved robustness and efficiency by leveraging sparse point correspondences and hierarchical representations. Prior-driven surface learning was further explored in PSDF [31], which injects geometric priors into implicit learning for better multi-view reconstruction. In parallel, scalable formulations like [32] addressed the challenge of high-quality reconstruction in large-scale settings, improving both accuracy and training efficiency. Complementary to these, decomposition-based formulations such as DM-NeRF [33] enabled geometry decomposition and manipulation directly from 2D images, highlighting the potential of scene factorization for enhancing surface-aware neural rendering.

Accelerated frameworks such as Instant-NGP [34] and Neuralangelo [35] utilized multi-resolution hash grids and coarse-to-fine optimization strategies to enhance detail recovery and computational efficiency. Meanwhile, task-specific extensions emerged, for example H₂O-NeRF [36] tailored radiance field reconstruction to the special case of two-hand-held objects, demonstrating the adaptability of neural implicit surfaces to constrained domains.

3DGSR [16] was one of the first methods to integrate SDFs directly with 3D Gaussian Splatting (3DGS) to enforce surface constraints while maintaining rendering speed. This approach introduced loose coupling strategies to align Gaussian primitives with SDF-derived surfaces, achieving a more detailed reconstruction than previous density-based methods. Despite the notable progress, the scalability and computational efficiency of these methods remained a challenge, particularly for large-scale and high-resolution scenes. For instance, BakedSDF [37] and NeRFMeshing [38] require hours of training and struggle with efficiently handling large-scale scene reconstruction.

Recent advancements, such as H3DNet [39], further emphasize the importance of geometric priors to stabilize the optimization of neural implicit surfaces, ensuring both geometric accuracy and robustness. Scaffold-GS [40] introduced hierarchical Gaussian structures for better alignment with scene geometry, but these approaches still face significant trade-offs between surface accuracy and computational efficiency.

B. Gaussian Splatting Based Surface Reconstruction

The introduction of 3D Gaussian Splatting (3DGS) [1], [41], [42] marked a breakthrough in real-time rendering for neural surface reconstruction, by representing scenes as sets of anisotropic Gaussians that can be rasterized efficiently. While 3DGS excels in rendering photorealistic images, it inherently struggles with geometric accuracy due to the unstructured nature of Gaussian primitives. Early attempts to reconcile rendering efficiency with surface quality include methods like SuGaR [15], which employed Poisson reconstruction, and 2DGS [13], which collapsed 3D Gaussians into planar surfels. These methods improved the overall quality but failed to preserve fine details or handle complex geometries.

NeuSG [43] and GOF [12] explored hybrid implicit-explicit paradigms by using SDFs or opacity fields to guide the placement of Gaussians. However, they face critical limitations, particularly in the alignment between the Gaussian primitives and the underlying surface. For example, Scaffold-GS [40] improved the structural alignment of the Gaussians but sacrificed high-frequency details, while PGSR [40] used planar decomposition techniques that limited the adaptability of the approach to more complex topologies.

3DGSR [16] proposed loose coupling strategies to align Gaussians with SDF-derived surfaces, enhancing the detail of the reconstruction while maintaining rendering efficiency. However, 3DGSR still faced challenges in achieving full geometric coverage and handling sparse data effectively.

Beyond these hybrid paradigms, several recent works expanded the scope and adaptability of 3DGS to various scenarios. MPGS [44] introduced a multi-plane Gaussian representation to improve compact scene rendering, while LoopSparseGS [45] proposed loop-based strategies for sparse-view friendly reconstruction. Fov-GS [46] leveraged foveated rendering to enable efficient handling of dynamic scenes, and RGAAvatar [47] extended Gaussian splatting to relightable 4D human avatar modeling. Similarly, PIGS [48] addressed robust panoptic lifting, and Look-at-the-Sky [49] specialized Gaussian splatting for outdoor environments. iVR-GS [50] explored editable and explorable visualization via inverse volume rendering, and ARAP-GRF [51] integrated deformation models for as-rigid-as-possible Gaussian field editing.

GSDF [17] later unified 3D Gaussian Splatting with SDFs through mutual geometry supervision, offering an improved surface representation. However, GSDF still struggled with computational efficiency and could not completely resolve issues related to large-scale scene reconstruction. GARF [52] introduced geometry-aware Gaussian refinement, but this method retained computational bottlenecks due to iterative density refinement processes.

These existing methods highlight the need for a framework that can tightly couple geometry and appearance while preserving the computational efficiency of 3D Gaussian Splatting. Our work in DiGS directly addresses these challenges by integrating SDF learning with 3D Gaussian Splatting in a unified manner. By combining normal-aligned growth and depth-guided grid expansion, DiGS ensures accurate surface reconstruction, robust spatial coverage, and high rendering efficiency. This innovative approach not only enhances geometric fidelity but also provides a scalable solution for textureless scenes, addressing the limitations of previous methods.

III. PRELIMINARY

a) 3D Gaussian Splatting: 3D Gaussian Splatting (3DGS) [1] represents a scene as a collection of spatially distributed anisotropic 3D Gaussians $\{\mathcal{G}_i\}_{i=1}^N$, where each primitive is parameterized by its center $\mathbf{p}_i \in \mathbb{R}^3$, a covariance matrix $\Sigma_i \in \mathbb{R}^{3 \times 3}$, color $\mathbf{c}_i \in \mathbb{R}^3$, and opacity $\alpha_i \in [0, 1]$. The covariance matrix is typically factorized into a scaling and rotation component to define elliptical spatial support.

To render an image, each Gaussian is projected into screen space, and its contribution is accumulated via front-to-back α -compositing:

$$\mathbf{C}(\mathbf{u}) = \sum_{i \in \mathcal{N}} T_i \alpha_i \mathbf{c}_i, \quad T_i = \prod_{j=1}^{i-1} (1 - \alpha_j), \quad (1)$$

where \mathcal{N} denotes the sorted set of Gaussians affecting pixel \mathbf{u} , and T_i represents the transmittance.

While 3DGS delivers photorealistic rendering with real-time performance, it lacks explicit geometric structure, and its opacity-driven formulation provides limited surface-awareness. Our work builds on this foundation by embedding signed distance priors directly into the Gaussian representation, enabling explicit surface alignment while preserving rendering efficiency.

b) Surface Regularization: To enhance geometric fidelity in multi-view reconstruction, recent methods introduce regularization objectives that enforce consistency across spatial and photometric domains. For instance, PGSR [14] proposes a composite geometric loss L_{geo} consisting of: (i) single-view geometric priors L_{svgeo} , (ii) multi-view geometric consistency L_{mvgeo} , and (iii) photometric alignment loss L_{mvrngb} . These constraints improve robustness in untextured regions and guide reconstructions toward structurally plausible surfaces.

Instead of optimizing loss terms post hoc, our framework integrates geometric priors directly into the representation by learning signed distance values at each Gaussian center, inherently encoding surface proximity and enabling structure-aware supervision during rendering and growth.

IV. METHOD

We propose DiGS, a unified framework that tightly couples implicit surface modeling with explicit radiance representation under the Gaussian splatting paradigm. Rather than treating geometry and appearance as disjoint components, DiGS embeds a Signed Distance Field (SDF) directly into each Gaussian primitive, and integrates a multi-scale Level-of-Detail (LoD) structure with a geometry-guided growth strategy. In this way, surface priors are inherently encoded within the rendering process, leading to precise surface alignment and efficient, adaptive scene representation. Importantly, all components of our approach are co-designed and jointly optimized end-to-end. This is in stark contrast to prior methods like GSDF [17], which separate geometry and radiance into dual branches, or Octree-GS [53] and PGSR [14], which perform multi-resolution refinement as a post-process. By unifying these aspects in a single pipeline, our method ensures that geometry and appearance remain consistent and mutually reinforcing throughout optimization. We next detail each part of the method, organized as follows: an SDF-Gaussian representation (IV-A) defines our base scene parameterization, a geometry-guided grid growth mechanism (IV-B) progressively refines this representation, and a set of optimization objectives (IV-C) enforces geometric fidelity and photometric accuracy.

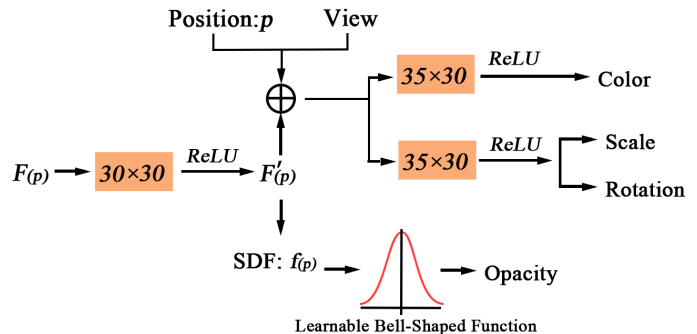


Fig. 3. Network Architecture. Given Gaussian position and view direction as inputs, an MLP predicts radiance features and signed distance values. The SDF is mapped to opacity through a learnable transfer function, ensuring surface awareness, while the radiance branch produces color for rendering.

A. Unified SDF-Gaussian Representation

Our scene representation augments each Gaussian splat with an explicit SDF value and is structured in a multi-scale fashion. This SDF-Gaussian representation provides a common foundation for modeling both surface geometry and appearance. Unlike approaches that simply combine separate modules, we design this representation as a unified structure. In particular, the SDF at each Gaussian influences its rendering opacity, and the LoD hierarchy is built to accommodate the SDF-guided growth of Gaussians.

1) Octree-Based LoD Initialization: To efficiently cover scenes at multiple scales, we begin by partitioning space with a hierarchical octree grid. Each octree level $\ell = 0, 1, \dots, L_{\text{max}}$ corresponds to a voxel size:

$$s_\ell = s_0 \cdot 2^\ell. \quad (2)$$

where s_0 is the base voxel size. Coarser levels (small ℓ) thus span larger regions with fewer primitives, while finer levels (large ℓ) focus on local details. We choose the number of levels L_{max} based on scene complexity and desired detail.

This ensures we capture fine details without an excessive number of primitives. The LoD structure enables adaptive refinement: broad areas are first represented coarsely, and only regions with complex geometry receive finer subdivisions. We initialize the octree using a sparse Structure-from-Motion (SfM) point cloud, which provides an initial approximation of scene geometry. Starting from the root (level 0) covering the entire scene, we subdivide octree cells down to a certain depth where sufficient SfM points fall inside. This yields an initial set of occupied voxels across levels, giving low-resolution coverage of the scene. Notably, the LoD grid in DiGS is not a fixed, static structure: it will be dynamically updated during training by our growth procedure.

2) Gaussian Position Encoding: Within each occupied octree cell, we allocate a small set of Gaussian primitives to represent local geometry and appearance. Specifically, each voxel at level ℓ is associated with k Gaussians (with k is 10 in our implementation). We parameterize the positions of these Gaussians relative to the voxel center \mathbf{x}_v as:

$$\{\mathbf{p}_0, \dots, \mathbf{p}_{k-1}\} = \mathbf{x}_v + \{\mathcal{C}_0 \cdot \mathcal{L}_0, \dots, \mathcal{C}_{k-1} \cdot \mathcal{L}_{k-1}\}. \quad (3)$$

where each $C_i \in \mathbb{R}^3$ is a learnable offset and $L_i \in \mathbb{R}^3$ is a learnable scale factor. Intuitively, C_i and L_i allow each Gaussian to shift from the cell center and spread around the voxel. This neural position encoding grants the model flexibility to fit complex local surface geometry: by adjusting the offsets, multiple Gaussians in a cell can align along different surface structures.

Each Gaussian is also associated with additional properties, such as a color and an anisotropic covariance matrix that defines its spatial extent. This design is crucial for capturing high-frequency geometry in regions of interest while keeping less interesting regions coarse. It also naturally complements the LoD structure by allowing newly subdivided cells to inherit and refine the features from their parent cell.

At any 3D Gaussian primitive center \mathbf{p} , we can query the neural grid features via interpolation. We employ an inverse distance weighting (IDW) scheme to aggregate features from nearby voxel centers. Specifically, we find the eight surrounding grid vertices that form the corners of the cell containing \mathbf{p} at the appropriate LoD level, and compute an interpolated feature $F(\mathbf{p})$ as:

$$F(\mathbf{p}) = \sum_{i=1}^8 \frac{w_i}{\sum_j w_j} f'_i, \quad \text{where } w_i = \frac{1}{\|\mathbf{x}_i - \mathbf{p}\| + \epsilon}. \quad (4)$$

where f_i is the feature stored at vertex \mathbf{x}_i , and ϵ is a small constant for numerical stability. This weighted sum smoothly blends the features of the nearby Gaussians or grid nodes, ensuring that $F(\mathbf{p})$ changes continuously as \mathbf{p} moves through space. We then decode $F'(\mathbf{p})$ from $F(\mathbf{p})$ via MLP and directly split the one-dimensional value of the decoded neural Gaussian Primitive feature $F'(\mathbf{p})$ as the SDF value $f(\mathbf{p})$, the whole process is shown on Figure 3.

3) *SDF Supervision and Opacity Modulation*: To infuse geometric awareness into each Gaussian, we assign a Signed Distance value to its center. Let $f(\mathbf{p})$ denote the signed distance from point \mathbf{p} to the nearest surface in the scene, with the convention that $f(\mathbf{p}) = 0$ on the surface, $f(\mathbf{p}) > 0$ outside (in free space), and $f(\mathbf{p}) < 0$ inside solid regions. In our representation, each Gaussian center \mathbf{p}_i carries a learnable parameter $f_i \approx f(\mathbf{p}_i)$ that estimates the true SDF at that location. The collection of all Gaussians' SDFs thus implicitly defines the scene's surface as the zero-level set:

$$\mathcal{S} = \{\mathbf{p} \in \mathbb{R}^3 \mid f(\mathbf{p}) = 0\}. \quad (5)$$

which we aim to reconstruct accurately. During training, we provide SDF supervision to guide f_i toward this true signed distance field (details in Sec. IV-C1), effectively encoding strong geometric priors into the model. The result is that geometry is no longer an afterthought: it is a core part of the representation, directly influencing how each primitive is treated in rendering.

To make use of these SDF values in our differentiable rendering process, we introduce an SDF-guided opacity modulation for the Gaussians. In standard Gaussian splatting (3DGS), each Gaussian has an opacity that determines how much it contributes along a ray, but this opacity is typically learned as an independent parameter or derived from image

colors, offering only indirect geometric meaning. In DiGS, we compute each Gaussian's opacity α_i as a function of its SDF value f_i . Specifically, we define a smooth kernel that peaks when the Gaussian lies on the surface ($f_i = 0$) and decays as the Gaussian moves away from the surface:

$$\alpha_i = \exp\left(-\frac{f(p_i)^2}{\delta^2}\right). \quad (6)$$

where δ is a learnable bandwidth parameter controlling the sharpness of the decay. This SDF-to-opacity mapping is a differentiable function that effectively locks each Gaussian to the surface: Gaussians with $f_i \approx 0$ (near the surface) will have high opacity (contribute strongly to rendering), whereas Gaussians with large $|f_i|$ (far from the surface either outside or inside) become nearly transparent. By plugging this α_i into the volume rendering, we ensure that only surface-aligned primitives are visibly rendered, and any Gaussian that drifts off the surface will automatically diminish in influence. The parameter δ can be learned or set to a small value so that the opacity drops off quickly with distance, yielding a tight approximation of an actual surface.

Crucially, our framework directly couples geometry and appearance via SDF-modulated opacity, unifying radiance and surface representations in a single branch. Each Gaussian encodes both geometry and color, ensuring consistency without the dual pipelines and enforcement mechanisms required by GSDF [17]. This tight integration simplifies optimization, avoids geometry–appearance misalignments, and yields more coherent, cross-view consistent reconstructions.

B. Geometry-Guided Grid Growth

Even with multi-scale priors, an initial Gaussian grid may leave surfaces under-sampled, especially in weakly textured or SfM-sparse regions. To overcome this, DiGS employs a geometry-guided grid growth strategy that inserts new Gaussians during training based on depth and normal cues, ensuring accurate surface coverage. Unlike offline refinements, growth is integrated into end-to-end optimization, leveraging the LoD octree for placement and SDF/normal supervision for precision. The process follows three stages: (1) depth-normal estimation, (2) coarse-to-fine insertion, and (3) Progressive refinement with growth and pruning. Pseudocode is provided in Algorithm 1 for reference.

1) *Depth-Normal Estimation*: We trigger the growth procedure at a certain training iteration (in our implementation, at $t = 5000$ iterations). At that point, we leverage multi-view geometry from the input images to estimate dense depth and surface normal maps for each training view. For this purpose, we can employ a robust multi-view stereo technique or leverage the current state of the model itself. In our implementation, we found it effective to use a plane-guided depth estimation similar to the one in PGSR [14]: by enforcing local planarity and photometric consistency across views, we compute a dense depth map $D_i(u, v)$ and normal map $N_i(u, v)$ for each image V_i (where (u, v) are pixel coordinates). This process is akin to a one-pass stereo reconstruction from the images, and it benefits from the fact that by iteration 5000 our

Algorithm 1 Grid Growth Strategy

Require: Training views $\{V_i\}$, Depth/normal model, LoD octree, θ_{thresh} , s_{down} , Current iteration t

Ensure: Updated LoD structure

```

1: if  $t = 5000$  then           ▷ Trigger growth at iteration 5000
2:   for each view  $V_i \in \{V_i\}$  do
3:     Step 1: Generate depth/normal maps
4:      $D_i, N_i \leftarrow \text{DepthNormalEstimation}(V_i)$ 
5:     Step 2: Filter observations
6:     for each pixel  $p$  in  $D_i$  do
7:        $\mathbf{v} \leftarrow \text{ViewingDirection}(p)$ 
8:        $\mathbf{n} \leftarrow N_i(p)$ 
9:       if  $\arccos(|\mathbf{v} \cdot \mathbf{n}|) > \theta_{\text{thresh}}$  then
10:        Discard  $p$            ▷ Remove grazing angles
11:      end if
12:    end for
13:    Step 3: Back-project point cloud
14:     $\mathcal{P}_{\text{raw}} \leftarrow \text{Backproject}(D_i, V_i.\text{camera})$ 
15:     $\mathcal{P}_{\text{filtered}} \leftarrow \text{UniformDownsample}(\mathcal{P}_{\text{raw}}, s_{\text{down}})$ 
16:    Step 4: Insert into LoD
17:    for each point  $\mathbf{p} \in \mathcal{P}_{\text{filtered}}$  do
18:      for  $\ell = 0$  to  $L_{\text{max}}$  do           ▷ Coarse-to-fine
insertion
19:        Grid  $\leftarrow \text{FindGrid}(\mathbf{p}, \text{LoD}[\ell].\text{resolution})$ 
20:        if Grid not occupied then
21:          Initialize grid with center at
voxel.center
22:           $\mathbf{n}_i \leftarrow \text{Normal}(\mathbf{p}, N_i)$ 
23:           $\mathbf{x}_i, \mathbf{y}_i \leftarrow \text{OrthogonalTangents}(\mathbf{n}_i)$ 
24:           $\mathbf{R} \leftarrow [\mathbf{x}_i, \mathbf{y}_i, \mathbf{n}_i]$            ▷ Local frame
25:           $\Sigma \leftarrow \mathbf{R} \cdot \text{diag}(\sigma_t^2, \sigma_t^2, \sigma_n^2) \cdot \mathbf{R}^\top$ 
26:          for  $j = 1$  to  $k$  do
27:            InitializeGaussianGrid
28:            (position = Grid.center,
29:             covariance =  $\Sigma$ )
30:            grid.AddGaussian( $G_j$ )
31:          end for
32:          LoD $[\ell].\text{AddGrid}(\text{grid})$ 
33:          break           ▷ Insert at coarsest possible
level
34:        end if
35:      end for
36:    end for
37:  end for
38: end if

```

model’s poses and coarse shape are already reasonably aligned with the training images.

Once we have the depth D_i and normal N_i for a view v , we filter these observations to ensure we only add high-quality points. We iterate over each pixel $p = (u, v)$ and consider the depth value $d = D_i(u, v)$ with its corresponding normal $\mathbf{n} = N_i(u, v)$. We discard points that are likely erroneous or not robust:

$$\text{if } \arccos(|\mathbf{v} \cdot \mathbf{n}|) > \theta_{\text{thresh}}, \quad \text{discard point.} \quad (7)$$

if the normal \mathbf{n} is not consistent with the viewing direction,

or if the depth confidence is low. After filtering, we obtain a set of reliable surface points for each view. These points densely sample the scene surfaces as seen from that view.

2) *Aggressive Coarse-to-Fine Insertion:* With the collected 3D surface points from all views, we proceed to aggressively insert new Gaussians into our representation to cover these surfaces. The goal is to fill in any gaps in the current Gaussian set by using the depth-informed points as candidate locations for new primitives. A naive approach might add a Gaussian at the exact location of every point, but this could lead to an unmanageable number of primitives and a lot of redundancy. Instead, we insert points in a structured manner aligned with our LoD octree. For each candidate point \mathbf{p} (with normal \mathbf{n}), we traverse the LoD hierarchy from coarse to fine and determine where to place Gaussians such that all levels are appropriately populated:

LoD-Aware Placement: Starting at the coarsest level $\ell = 0$, we check if \mathbf{p} falls inside an existing voxel at that level that already contains a Gaussian. If not (meaning the coarse grid had a hole at that location), we create a new Gaussian grid cell at level 0 covering \mathbf{p} and initialize it with k Gaussians (distributed by the same offset scheme as before). We orient the covariance of these new Gaussians according to the normal \mathbf{n} , i.e., we align each new Gaussian’s principal axis with \mathbf{n} so that they lie roughly tangent to the surface. We also set the SDF values of these new Gaussians to $f \approx 0$ initially to integrate them smoothly into the model.

$$\Sigma = \mathbf{R} \begin{bmatrix} \sigma_t^2 & 0 & 0 \\ 0 & \sigma_t^2 & 0 \\ 0 & 0 & \sigma_n^2 \end{bmatrix} \mathbf{R}^\top, \quad \text{where } \mathbf{R} = [\mathbf{a}_i, \mathbf{b}_i, \mathbf{n}_i]. \quad (8)$$

Here, σ_t and σ_n denote the Gaussian radii in the tangent and normal direction. We set $\sigma_t = 1.0$ and $\sigma_n = 0.1$ to limit the expansion of the Gaussian along the normal. This design allows each Gaussian to capture local surface curvature and orientation, laying a geometry-aware foundation for subsequent optimization stages.

We then proceed to level $\ell = 1$: we find the child cell of the previously considered cell that contains \mathbf{p} , and similarly check if that child exists. If not, we insert a new cell at level 1 with Gaussians (again oriented by \mathbf{n}). We repeat this process for each level up to $\ell = L_{\text{max}}$. In essence, each point \mathbf{p} can spawn at most one new cell per level, ensuring that all scales have a representation of that surface point if it was missing. If at some level the cell already existed (because perhaps another nearby point already triggered its creation or it was present from initialization), we skip adding at that level to avoid duplicates.

Avoiding Redundancy: This coarse-to-fine insertion ensures hierarchical consistency: a newly added fine Gaussian will also have support from coarser levels. By design, we do not add a new Gaussian into an occupied voxel to avoid redundant representations. This strategy contrasts with a naive global insertion of points which could clump many Gaussians in an area already represented. By checking occupancy at each level, we keep the Gaussian distribution even and controlled. Moreover, inserting from coarse to fine allows the model

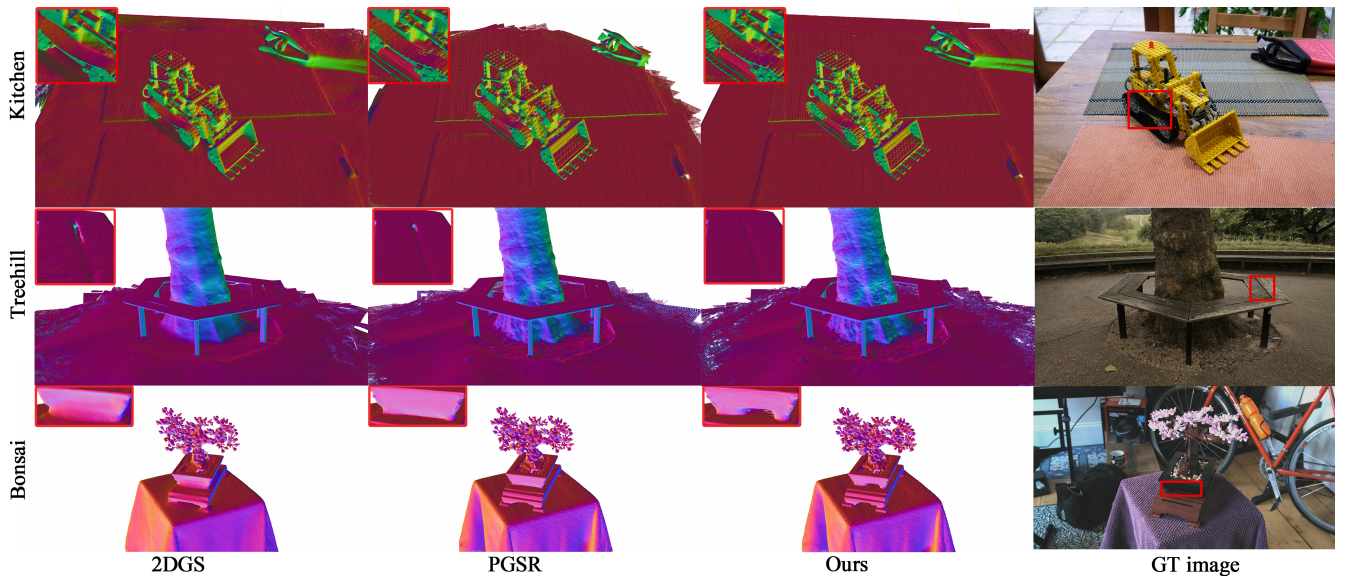


Fig. 4. The Qualitative Results on the Mip-NeRF 360 dataset [54]. Our method demonstrates superior reconstruction quality, particularly in complex geometric regions and fine structural details as highlighted by the red box.

to maintain approximate coverage at all scales, which is important for both rendering.

After processing all candidate points in this manner, we update the LoD octree data structure to include all newly created cells and Gaussians. The result is a significantly densified Gaussian representation that now explicitly covers surfaces that were previously missed or under-sampled. We call this an “aggressive” growth because it can substantially increase the number of Gaussians in one go. However, because we insert guided by actual geometry and enforce the octree structure, the growth is targeted and does not lead to gratuitous increase in regions that were already adequately modeled.

3) *Progressive Growth and Pruning*: After the aggressive insertion step, we resume the end-to-end training of the model with the expanded set of Gaussians. To handle the sudden increase in parameters, we employ a progressive learning rate schedule: we temporarily boost the learning rate for the newly added Gaussians’ parameters while slightly reducing it for the pre-existing ones, ensuring the new Gaussians quickly adjust to integrate with the scene without disturbing the already learned structure. Over time, these learning rates are unified again as the new primitives become part of the model. This strategy helps maintain training stability during growth.

As training continues, the new Gaussians will have their SDF values and colors refined by the loss functions (Sec. IV-C), and any initial errors in their placement will be corrected. Because we inserted Gaussians at all LoD levels for each point, the model can learn a consistent multi-scale representation of newly added regions: coarse new Gaussians ensure that even from distant viewpoints the region contributes, while fine ones add detail up close. The LoD coupling also means that our earlier interpolation scheme and SDF field remain continuous despite the insertions, we added features at new grid vertices, and our IDW interpolation naturally incorporates those when querying points in those regions.

To keep the model efficient, we also perform pruning of

redundant or unhelpful Gaussians as training proceeds. In particular, if a coarse Gaussian’s region has been completely taken over by finer Gaussians, we can safely deactivate or remove that coarse Gaussian. This pruning prevents double-counting of contributions and focuses computation on the needed primitives. Similarly, if any Gaussian satisfies both low opacity ($\alpha < \tau_\alpha$) or the signed distance ($|\text{SDF}| > \tau_{\text{sdf}}$), we can remove it from the model to streamline the representation. This keeps the scene representation compact and clean, containing mostly surface-relevant Gaussians.

C. Optimization and Loss Functions

With the representation and growth strategy defined, we now describe the optimization objectives that guide the training of DiGS. Our loss design follows the principle of treating geometry as a first-class objective, while also ensuring high-quality radiance reconstruction. We employ a set of complementary losses: (1) geometric losses that supervise the SDF values and enforce SDF properties, (2) a flattening loss that regularizes Gaussian shape along surfaces, (3) an appearance loss for RGB reconstruction, and (4) a combined objective that balances all terms. Each loss term plays a specific role, and importantly, they act in concert on our unified pipeline. This means, for example, that improving geometric alignment via SDF losses also immediately benefits the rendering, and vice versa. We detail each category of loss below.

1) *Geometric Losses*: To supervise the SDF values attached to Gaussians, we design losses that encourage those values to reflect true surface distances and to satisfy the mathematical properties of an SDF. First, we introduce an SDF center loss L_{SDF} that penalizes the absolute SDF value at any Gaussian which is expected to lie on the surface. Concretely, for each Gaussian i that corresponds to a measured surface point, we add a term $|f(p_i) - 0|$ to the loss. We determine which

TABLE I

QUANTITATIVE RESULTS OF CHAMFER DISTANCE (MM) ON DTU DATASET. OUR METHOD OUTPERFORMS EXISTING 3D GS AND NeRF-BASED APPROACHES, ACHIEVING STATE-OF-THE-ART ACCURATE RECONSTRUCTION QUALITY ON THE DTU DATASET. "RED", "ORANGE" AND "YELLOW" DENOTE THE BEST, SECOND-BEST, AND THIRD-BEST RESULTS.

Method	24	37	40	55	63	65	69	83	97	105	106	110	114	118	122	Mean	Time
VolSDF	1.14	1.26	0.81	0.49	1.25	0.70	0.72	1.29	1.18	0.70	0.66	1.08	0.42	0.61	0.55	0.86	>12h
NeuS	1.00	1.37	0.93	0.43	1.10	0.65	0.57	1.48	1.09	0.83	0.52	1.20	0.35	0.49	0.54	0.84	>12h
Neuralangelo	0.37	0.72	0.35	0.35	0.87	0.54	0.53	1.29	0.97	0.73	0.47	0.74	0.32	0.41	0.43	0.61	>128h
SuGaR	1.47	1.33	1.13	0.61	2.25	1.71	1.15	1.63	1.62	1.07	0.79	2.45	0.98	0.88	0.79	1.33	1h
GSDF	0.59	0.94	0.46	0.38	1.30	0.77	0.73	1.59	1.29	0.76	0.59	1.22	0.38	0.52	0.51	0.80	>2h
Scaffold-GS	7.23	6.23	6.48	7.44	8.17	4.27	5.78	5.45	6.57	6.36	5.05	5.95	6.32	5.62	2.90	4.63	0.8h
Octree-GS	4.3	3.45	4.56	3.45	5.67	2.345	3.45	4.45	3.32	3.35	2.45	4.56	4.45	3.45	4.34	4.23	0.7h
2DGS	0.46	0.91	0.39	0.39	1.01	0.83	0.81	1.36	1.27	0.76	0.70	1.40	0.40	0.76	0.52	0.80	0.32h
GOF	0.50	0.82	0.37	0.37	1.12	0.74	0.73	1.18	1.29	0.68	0.77	0.90	0.42	0.66	0.49	0.74	2h
PGSR	0.34	0.58	0.29	0.29	0.78	0.58	0.54	1.01	0.73	0.51	0.49	0.69	0.31	0.37	0.38	0.53	1h
Ours	0.45	0.44	0.25	0.33	0.69	0.49	0.46	0.92	0.57	0.47	0.43	0.46	0.28	0.35	0.32	0.46	1.2h

TABLE II

QUANTITATIVE RESULTS OF RECONSTRUCTION ON TNT DATASET [55].

Scene	NeuS	Geo-Neus	Neuralangelo	2D GS	GOF	PGSR	Ours
Barn	0.29	0.33	0.70	0.36	0.44	0.66	0.68
Caterpillar	0.29	0.26	0.36	0.23	0.41	0.41	0.42
Courthouse	0.17	0.12	0.28	0.13	0.28	0.21	0.25
Ignatius	0.83	0.72	0.89	0.44	0.68	0.80	0.83
Meetingroom	0.24	0.20	0.32	0.16	0.28	0.29	0.28
Truck	0.45	0.45	0.46	0.26	0.58	0.60	0.61
Mean	0.38	0.35	0.50	0.30	0.46	0.50	0.51

TABLE III

PERFORMANCE COMPARISON OF NOVEL VIEW SYNTHESIS ON MIP-NeRF 360 DATASET [54]. OUR METHOD HAS A STRONG PERFORMANCE.

Method	Indoor Scenes			Outdoor Scenes			All Scenes		
	PSNR↑	SSIM↑	LPIPS↓	PSNR↑	SSIM↑	LPIPS↓	PSNR↑	SSIM↑	LPIPS↓
NeRF	26.84	0.790	0.370	21.46	0.458	0.515	24.15	0.624	0.443
Deep Blending	26.40	0.844	0.261	21.54	0.524	0.364	23.97	0.684	0.313
Instant-NGP	29.15	0.880	0.216	22.90	0.566	0.371	26.03	0.723	0.294
Mip-NeRF360	31.72	0.917	0.180	24.47	0.691	0.283	28.10	0.804	0.232
NeuS	25.10	0.789	0.319	21.93	0.629	0.600	23.74	0.720	0.439
3DGS	30.99	0.926	0.199	24.24	0.705	0.283	27.24	0.803	0.246
2DGS	30.39	0.923	0.183	24.33	0.709	0.284	27.03	0.804	0.239
SuGaR	29.44	0.911	0.216	22.76	0.631	0.349	26.10	0.771	0.283
GOF	30.80	0.928	0.167	24.76	0.742	0.225	27.78	0.835	0.196
PGSR	30.41	0.930	0.161	24.45	0.730	0.224	27.43	0.830	0.193
Ours	30.60	0.927	0.171	24.73	0.739	0.254	27.67	0.833	0.212

Gaussians should lie on the surface. Then:

$$\mathcal{L}_{\text{SDF-Center}} = \sum_i |f(p_i)|^2. \quad (9)$$

driving those $f(p_i)$ to zero. Next, we impose the Eikonal loss [56] to ensure the learned SDF behaves like a true signed Distance Field in the continuous space. The Eikonal term enforces that the gradient magnitude of $f(\mathbf{p})$ is 1 everywhere (which is a defining property of distance fields). We then add:

$$\mathcal{L}_{\text{Eikonal}} = \mathbb{E}_{\text{pix} \sim \mathcal{X}} (\|\nabla f(p)\|_2 - 1)^2. \quad (10)$$

which encourages $|\nabla f| = 1$. This regularizes the SDF field to prevent pathological solutions (e.g., constant or zero everywhere) and promotes smoothness in geometry. It also couples with the SDF center loss: having $f = 0$ at surface points and unit gradient means that nearby points will get correct sign distances. Overall, these geometric losses provide strong supervision of the SDF compared to prior methods: for example, PGSR [14] used normal consistency losses indirectly, whereas we directly learn the SDF which inherently encodes surface normals (via ∇f) and distances. By integrating this

into our pipeline, we ensure multi-view geometric consistency is achieved through the SDF representation itself, rather than requiring separate multi-view consistency losses. This simplifies the training and yields a more interpretable geometric model as a byproduct. The overall SDF consistency can be geometrically regularized to:

$$\mathcal{L}_{\text{SDF}} = \lambda_4 \mathcal{L}_{\text{sdf-center}} + \lambda_5 \mathcal{L}_{\text{Eikonal}}. \quad (11)$$

λ_4 and λ_5 are the parameters of the corresponding loss.

2) *Flattening Loss for Gaussian Covariance*: Each Gaussian is an anisotropic ellipsoid parameterized by covariance $\Sigma_i = \mathbf{R}_i \mathbf{S}_i \mathbf{S}_i^\top \mathbf{R}_i^\top$, where $\mathbf{R}_i \in \mathbb{R}^{3 \times 3}$ is a rotation matrix and $\mathbf{S}_i = \text{diag}(s_{i1}, s_{i2}, s_{i3})$ scales along principal axes. Following [13], the smallest scale direction defines the local surface normal \mathbf{n}_i . Minimizing this smallest scale encourages flattening along \mathbf{n}_i , promoting compact, planar Gaussians:

$$\mathcal{L}_s = \lambda_6 \sum_i \min(s_4, s_5, s_6).$$

3) *RGB Reconstruction Loss*: For appearance, we use an RGB reconstruction loss to train the color output of our model. We render each training image via our differentiable splatting (with SDF-based opacities) and compare to the ground truth image. We denote by $C_i(u, v)$ the color predicted by our model for pixel (u, v) in view V_i , and $C_i^{GT}(u, v)$ the corresponding ground truth pixel color. We then define:

$$\mathcal{L}_{\text{rgb}} = (1 - \lambda_7) \|\tilde{I} - I_i\|_1 + \lambda_7 \cdot \text{SSIM}(\tilde{I}, I_i). \quad (12)$$

where \tilde{I} denotes the rendered image, I_i denotes the ground truth image and λ_7 controls the trade-off.

4) *Final Objective*: The total loss is a weighted sum of the above terms:

$$\mathcal{L} = \mathcal{L}_{\text{rgb}} + \mathcal{L}_s + \mathcal{L}_{\text{geo}} + \mathcal{L}_{\text{SDF}}. \quad (13)$$

V. EXPERIMENT

A. Experimental Setup

Datasets and Baselines. We evaluate our method on three diverse datasets: DTU [57], Mip-NeRF 360 [54], TnT [55]. These datasets cover a range of 3D scene complexities, providing a comprehensive benchmark for reconstruction accuracy

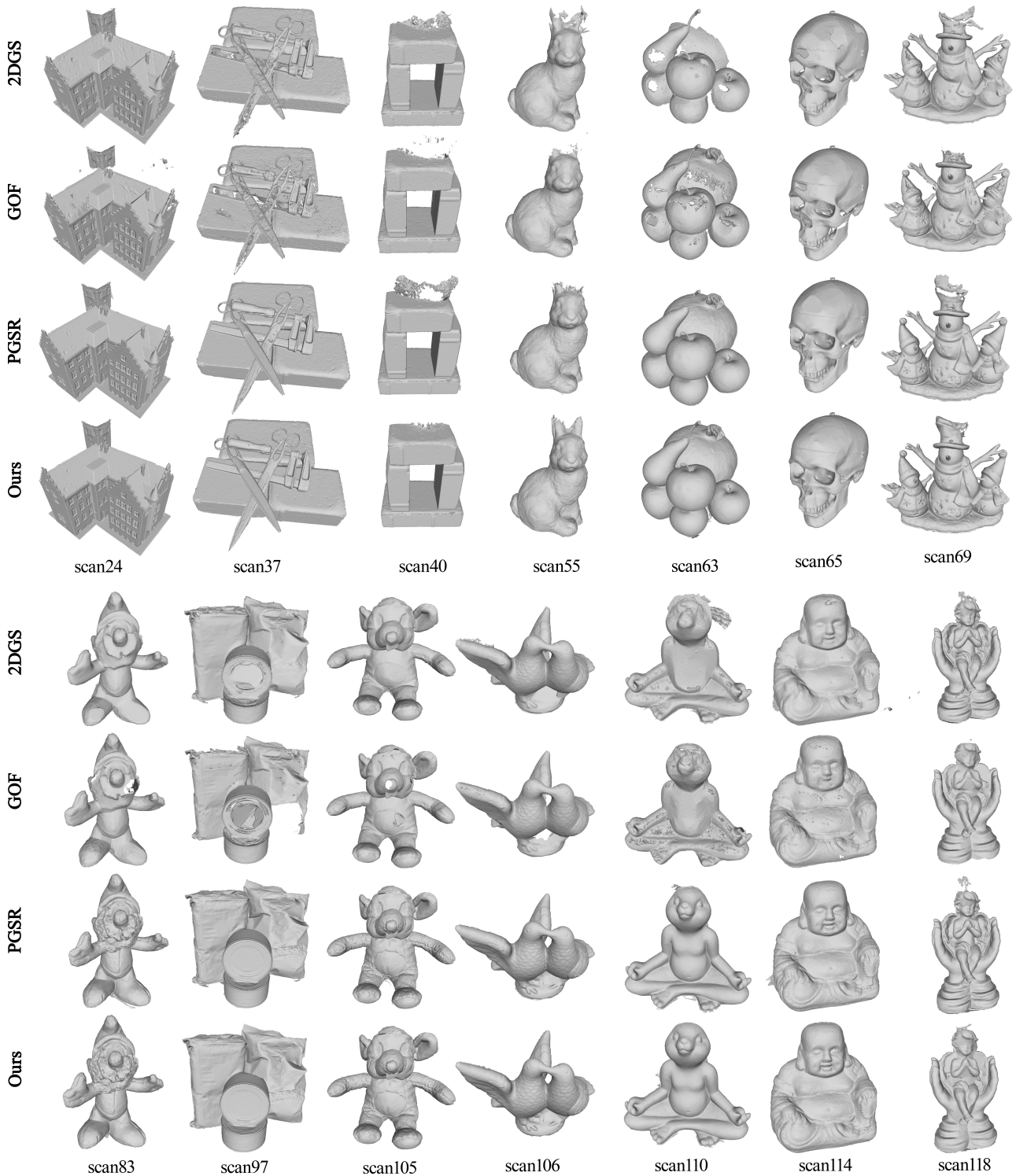


Fig. 5. The Qualitative Results on DTU dataset. Our method has more complete and accurate reconstruction results in scenes scan40, scan55, and scan69, and better reconstruction details in scan37, scan65, and scan110.

and visual fidelity. For comparison, we select a set of state-of-the-art reconstruction methods: NeRF [18], NeuS [19], Neuralangelo [35], Deep Blending [58], INGP [34], 3DGS [1], Scaffold-gs [40], Octree-gs [53], SuGar [15], and PGSR [14], each representing a notable approach in 3D scene surface reconstruction.

Evaluation Metrics. We assess the performance of our

method using several standard reconstruction and rendering metrics: Chamfer Distance, F1-score, along with image quality metrics including PSNR, SSIM, and LPIPS. These metrics allow for a holistic evaluation of both geometric fidelity and photorealistic rendering quality. Mesh reconstruction is achieved using a TSDF-based extraction method [14], which ensures consistency in the surface.

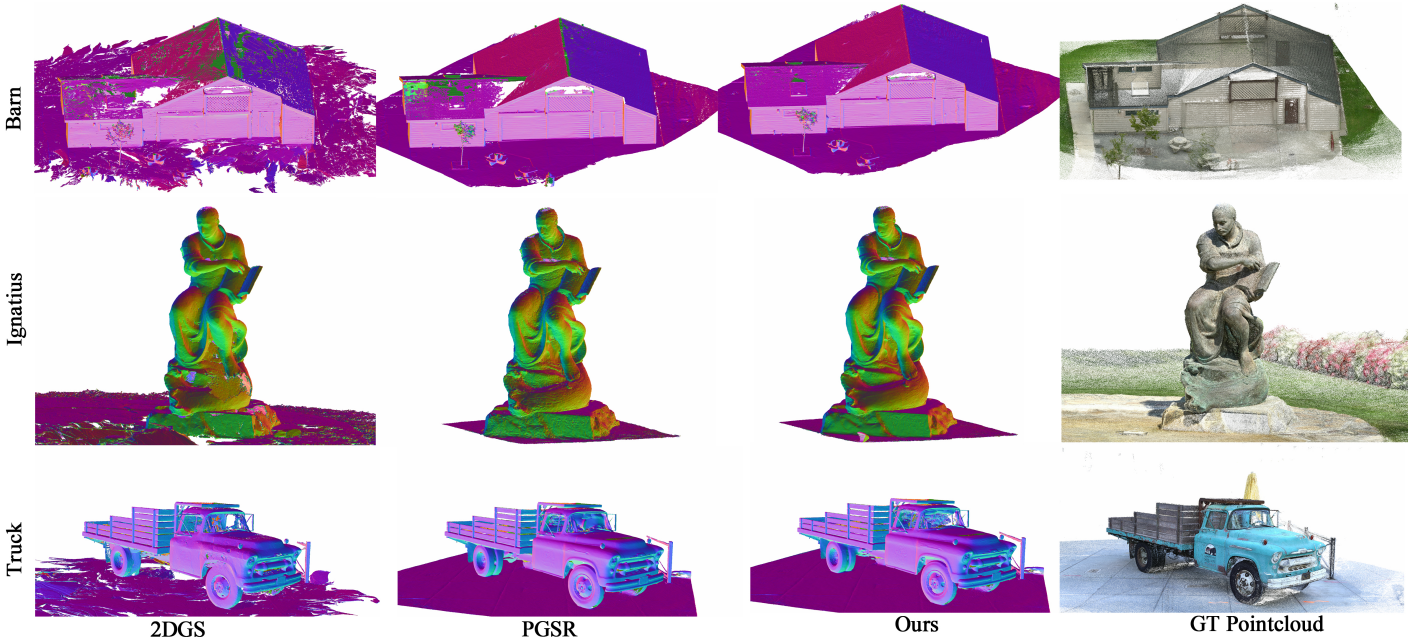


Fig. 6. The Qualitative Comparison of Reconstruction Results on the Truck, Ignatius, and Barn scenes from the TnT Dataset [55]. Our method demonstrates superior fidelity in preserving geometric details and structural integrity. Notably, our approach achieves sharper edges, and more consistent surface continuity.

Implementation Details. The optimization process incorporates multiple loss components, including L1 loss, SSIM loss, image photometric loss, Gaussian flattening loss, single-view loss, and multi-view loss. The corresponding weight factors, λ_4 to λ_7 , are set to 0.01, 0.01, 100, and 0.05, respectively. These weights are carefully tuned to balance the contributions of each loss term, ensuring optimal convergence and faithful reconstruction throughout the training process.

Our training follows the schedule outlined in 3D Gaussian Splatting, with a total of 30,000 epochs. The densification process begins at epoch 1500 and concludes at epoch 15,000, facilitating gradual scene refinement. To enhance geometric accuracy in sparse regions, the depth-aggressive growth strategy is activated at epoch 5,000. We employ a progressive learning rate schedule for neural network components, gradually increasing their learning capacity over time, while maintaining a fixed learning rate for the grid positions to preserve spatial stability throughout training.

All experiments are conducted on a single NVIDIA RTX 3090 GPU. For large-scale datasets that exceed the GPU memory capacity, data loading is offloaded to the CPU. This strategy mitigates GPU memory pressure, ensuring stable training throughput and the ability to handle larger datasets without compromising performance.

B. Reconstruction

Accuracy. We evaluate reconstruction accuracy on both DTU [57] and Tanks & Temples (TnT). Table I reports Chamfer Distance on DTU, where our method achieves the lowest error among all compared approaches, clearly outperforming Gaussian-based 3DGS [1] and neural implicit baselines such as NeRF [18] and NeuS [19]. Table II further presents F1 scores on TnT, which jointly capture precision and recall under

a strict distance threshold. Our method consistently achieves the highest average F1, indicating both accurate alignment to ground truth geometry and reliable coverage of fine details. These results demonstrate that explicitly embedding signed distance supervision into Gaussian primitives significantly improves geometric fidelity across benchmarks.

Qualitative results corroborate the quantitative improvements. As shown in Figures 4, 5, and 6, our reconstructions exhibit sharper boundaries, cleaner topology, and better preservation of thin structures compared to competing methods. In contrast, baselines such as GOF [12] often display surface drift, misalignments, or incomplete recovery, particularly in regions with fine-scale details or weak textures. Our method also generalizes robustly to real-world Mip-NeRF 360 scenes, where it produces geometrically faithful surfaces despite complex illumination and scale variations.

Completeness. Beyond accuracy, we assess the completeness of reconstructed surfaces, which is particularly challenging in occluded or low-texture regions. Prior Gaussian-based pipelines often rely on appearance-driven growth strategies, resulting in uneven Gaussian distributions and noticeable holes. In contrast, our geometry-guided aggressive grid growth adaptively expands Gaussians along surface-consistent directions, ensuring dense coverage and robust scene reconstruction.

Figures 4 and 6 highlight this advantage: our method yields reconstructions with more uniform Gaussian placement and significantly fewer missing regions, even under severe occlusions or texture sparsity. Competing methods frequently fail to recover such areas, leaving gaps or fragmented structures, while our approach produces coherent and watertight models. These results confirm that the proposed growth mechanism plays a critical role in achieving visually complete reconstructions, complementing the quantitative accuracy improvements.

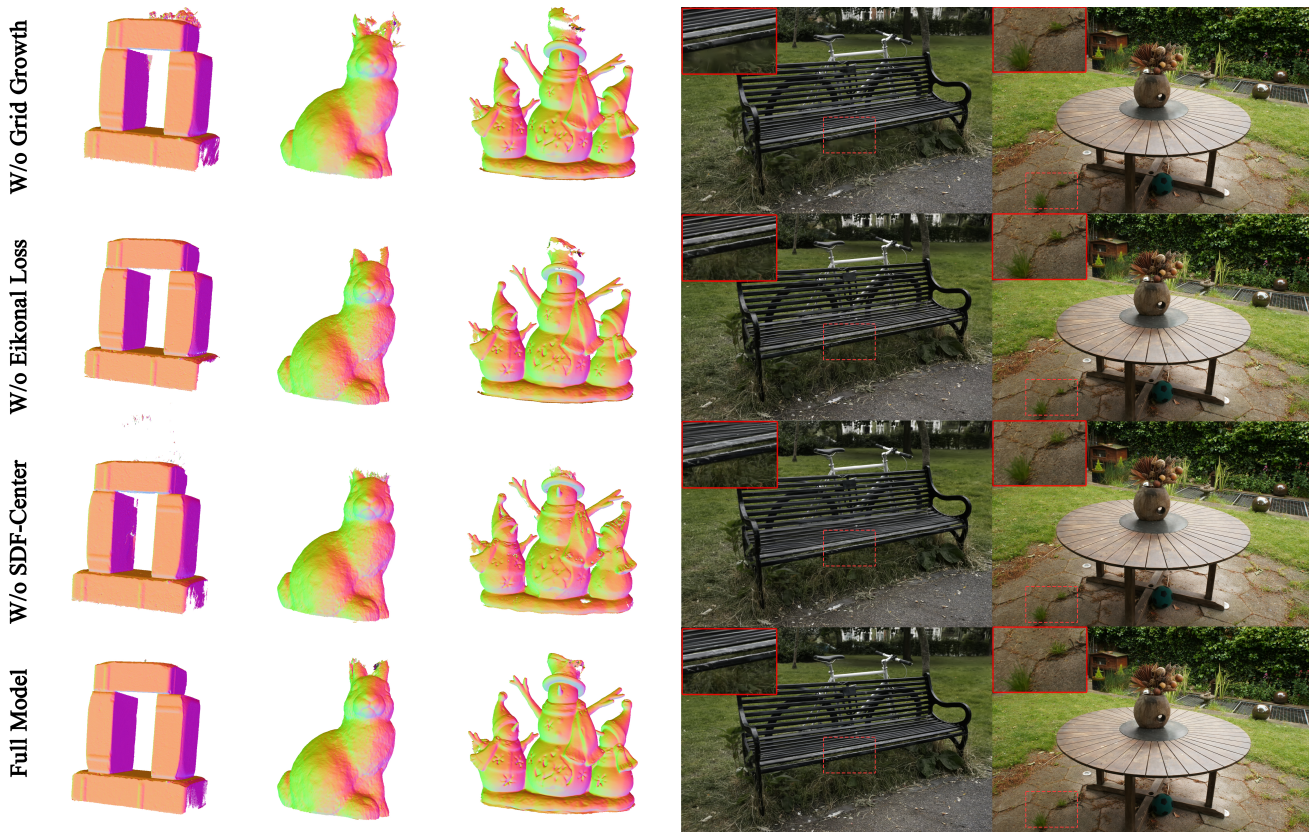


Fig. 7. Qualitative ablation on DTU [57] and Mip-NeRF360 [54]. Rows from top to bottom show the model without geometry-guided grid growth, without Eikonal loss, without SDF-center loss, and the full model. Left block shows reconstructed geometry with surface normals on DTU objects. Right block shows novel view synthesis results on Mip-NeRF360 with zoom-in insets. Removing any component degrades edge sharpness, normal consistency, and coverage, while the full model recovers thin structures and fills missing regions.

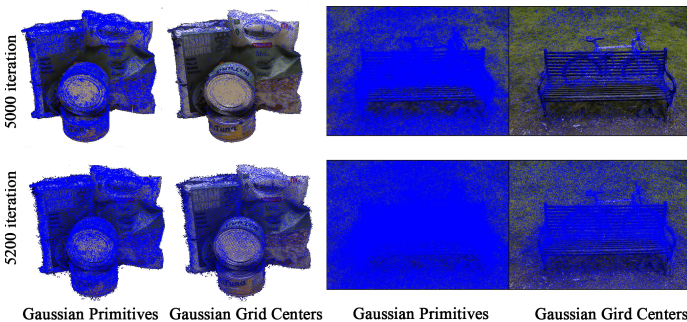


Fig. 8. The Process of Aggressive Grid Growth strategy. At 5000 iterations, the Grid Growth strategy is executed.

C. Novel View Synthesis

For the evaluation of novel view synthesis quality, we adopt the rigorous evaluation protocol established by 3DGS and conduct a comprehensive assessment on the Mip-NeRF360 [54] benchmark dataset. This allows us to thoroughly evaluate the proposed method’s performance in generating novel views from sparse input perspectives. To ensure a balanced and fair comparison, we benchmark our method against two categories of state-of-the-art (SOTA) approaches: (1) methods that have demonstrated exceptional performance in novel view synthesis

tasks and (2) surface reconstruction techniques that share similar technical principles with our framework.

As detailed in Table III, our approach not only excels in high-precision surface geometry reconstruction but also achieves remarkable performance in terms of visual quality metrics for novel view synthesis. This includes improvements in image fidelity, detail retention, and depth consistency when viewed from unseen viewpoints. The results clearly highlight that our method balances geometric accuracy with photo-realistic rendering quality, offering a more robust solution for novel view synthesis compared to existing techniques. These advancements are underpinned by the synergy between our SDF-constrained 3D Gaussian representation and adaptive grid growth strategy, which together enhance both geometric consistency and visual realism.

D. Ablation Study

We evaluate three principal design choices of our method: *SDF-constrained 3D Gaussians* enforced by an SDF-center loss, *Eikonal regularization* for gradient and normal consistency, and *geometry-guided aggressive grid growth* driven by depth and normal cues. Quantitative results on DTU and Mip-NeRF360 are reported in Table IV. Qualitative comparisons are shown in Fig. 7, and the growth schedule is illustrated in Fig. 8. Across both datasets, removing any single component consistently degrades geometric accuracy and perceptual

TABLE IV

QUANTITATIVE ABLATION ON DTU [57] AND MIP-NeRF360 [54]. THE FULL MODEL ACHIEVES THE BEST SCORES ON BOTH DATASETS, CONFIRMING THE COMPLEMENTARY EFFECTS OF SDF ANCHORING, EIKONAL REGULARIZATION, AND GEOMETRY-GUIDED AGGRESSIVE GRID GROWTH.

Method	DTU				Mip-NeRF360		
	CD↓	PSNR↑	SSIM↑	LPIPS↓	PSNR↑	SSIM↑	LPIPS↓
W/o SDF-Center constraint	0.49	34.65	0.74	0.370	27.43	0.828	0.217
W/o Eikonal Regularization	0.51	34.18	0.68	0.361	27.33	0.827	0.220
W/o Aggressive Grid Growth	0.50	34.13	0.70	0.317	27.45	0.826	0.227
Full Model	0.46	35.63	0.81	0.219	27.67	0.833	0.212

quality, which indicates complementary effects among the proposed modules.

a) SDF-constrained 3D Gaussians representation: Binding each Gaussian to the SDF zero level set through the center prior provides geometric anchoring that suppresses surface drift and floating artifacts. Without this loss, CD on DTU increases from 0.46 to 0.49, PSNR decreases from 35.63 to 34.65, and SSIM drops from 0.81 to 0.74. On Mip-NeRF360, PSNR declines from 27.67 to 27.43, SSIM from 0.833 to 0.828, and LPIPS rises from 0.212 to 0.217. Normal visualizations in Fig. 7 reveal softened edges and small-scale misalignments in high-curvature regions. These observations show that SDF anchoring turns Gaussians into surface-attached primitives rather than view-dependent volumetric proxies.

b) Eikonal regularization: The Eikonal term enforces unit SDF gradients and yields well-behaved normals and a thin, stable level set. Removing this regularization leads to over-smoothed geometry. On DTU, CD rises to 0.51, SSIM falls to 0.68, and PSNR decreases by 1.45 dB from 35.63 to 34.18. On Mip-NeRF360, PSNR reduces to 27.33, SSIM to 0.827, and LPIPS increases to 0.220. Visual evidence in Fig. 7 shows loss of crisp boundaries on the bench slats and the tabletop rim together with locally inconsistent normals. These results highlight the role of the Eikonal term in preserving fine detail and enforcing a coherent surface.

c) Geometry-guided aggressive grid growth: We introduce a one-shot aggressive expansion of the Gaussian grid scheduled at 5k iterations and guided by depth residuals and normal disagreement. In contrast to uniform or heuristic upsampling, this policy allocates new primitives only where geometry is under-explained, which rapidly covers unmodeled regions while avoiding redundant capacity in flat areas. Disabling this module reduces DTU SSIM from 0.81 to 0.70 and increases LPIPS from 0.219 to 0.317. On Mip-NeRF360, PSNR drops from 27.67 to 27.45, SSIM from 0.833 to 0.826, and LPIPS rises to 0.227. Fig. 7 shows incomplete coverage and gaps along thin structures such as bench slats and in low-texture ground regions when the growth policy is removed. The data indicate that deciding where and when to grow matters as much as the total amount of growth.

VI. CONCLUSION

We presented DiGS, a unified framework that embeds signed distance supervision directly into Gaussian primitives and integrates a geometry-guided grid growth strategy under a multi-scale hierarchy, thereby transforming Gaussian splatting

into a geometry-preserving paradigm. By tightly coupling geometry and appearance within a single optimization process, DiGS achieves accurate and complete surface reconstruction while retaining high-fidelity rendering. Extensive experiments validate that this joint design yields sharp structural details, robust surface consistency, and efficient scalability across diverse datasets. We envision future extensions of DiGS toward explicit mesh integration, dynamic scene modeling, and data compression, further broadening its applicability in real-time, geometry-aware 3D reconstruction.

REFERENCES

- [1] B. Kerbl, G. Kopanas, T. Leimkühler, and G. Drettakis, “3d gaussian splatting for real-time radiance field rendering,” *ACM Trans. Graph.*, vol. 42, no. 4, pp. 139–1, 2023.
- [2] H. Zhai, X. Zhang, B. Zhao, H. Li, Y. He, Z. Cui, H. Bao, and G. Zhang, “Splatloc: 3d gaussian splatting-based visual localization for augmented reality,” *IEEE Transactions on Visualization and Computer Graphics*, 2025.
- [3] H. Song, “Toward realistic 3d avatar generation with dynamic 3d gaussian splatting for ar/vr communication,” in *2024 IEEE Conference on Virtual Reality and 3D User Interfaces Abstracts and Workshops (VRW)*. IEEE, 2024, pp. 869–870.
- [4] Y. Jiang, C. Yu, T. Xie, X. Li, Y. Feng, H. Wang, M. Li, H. Lau, F. Gao, Y. Yang *et al.*, “Vr-gs: A physical dynamics-aware interactive gaussian splatting system in virtual reality,” in *ACM SIGGRAPH 2024 Conference Papers*, 2024, pp. 1–1.
- [5] H. Lian, K. Liu, R. Cao, Z. Fei, X. Wen, and L. Chen, “Integration of 3d gaussian splatting and neural radiance fields in virtual reality fire fighting,” *Remote Sensing*, vol. 16, no. 13, p. 2448, 2024.
- [6] X. Zhou, Z. Lin, X. Shan, Y. Wang, D. Sun, and M.-H. Yang, “Drivinggaussian: Composite gaussian splatting for surrounding dynamic autonomous driving scenes,” in *Proceedings of the IEEE/CVF conference on computer vision and pattern recognition*, 2024, pp. 21 634–21 643.
- [7] M. Khan, H. Fazlali, D. Sharma, T. Cao, D. Bai, Y. Ren, and B. Liu, “Autosplat: Constrained gaussian splatting for autonomous driving scene reconstruction,” *arXiv preprint arXiv:2407.02598*, 2024.
- [8] G. Hess, C. Lindström, M. Fatemi, C. Petersson, and L. Svensson, “Splatad: Real-time lidar and camera rendering with 3d gaussian splatting for autonomous driving,” *arXiv preprint arXiv:2411.16816*, 2024.
- [9] B. Fei, J. Xu, R. Zhang, Q. Zhou, W. Yang, and Y. He, “3d gaussian splatting as new era: A survey,” *IEEE Transactions on Visualization and Computer Graphics*, 2024.
- [10] K. Cheng, X. Long, K. Yang, Y. Yao, W. Yin, Y. Ma, W. Wang, and X. Chen, “Gaussianpro: 3d gaussian splatting with progressive propagation,” in *Forty-first International Conference on Machine Learning*, 2024.
- [11] T. Wu, Y.-J. Yuan, L.-X. Zhang, J. Yang, Y.-P. Cao, L.-Q. Yan, and L. Gao, “Recent advances in 3d gaussian splatting,” *Computational Visual Media*, vol. 10, no. 4, pp. 613–642, 2024.
- [12] Z. Yu, T. Sattler, and A. Geiger, “Gaussian opacity fields: Efficient adaptive surface reconstruction in unbounded scenes,” *ACM Transactions on Graphics (TOG)*, vol. 43, no. 6, pp. 1–13, 2024.
- [13] B. Huang, Z. Yu, A. Chen, A. Geiger, and S. Gao, “2d gaussian splatting for geometrically accurate radiance fields,” in *ACM SIGGRAPH 2024 conference papers*, 2024, pp. 1–11.

- [14] D. Chen, H. Li, W. Ye, Y. Wang, W. Xie, S. Zhai, N. Wang, H. Liu, H. Bao, and G. Zhang, "Pgsr: Planar-based gaussian splatting for efficient and high-fidelity surface reconstruction," *IEEE Transactions on Visualization and Computer Graphics*, 2024.
- [15] A. Guédon and V. Lepetit, "Sugar: Surface-aligned gaussian splatting for efficient 3d mesh reconstruction and high-quality mesh rendering," in *Proceedings of the IEEE/CVF Conference on Computer Vision and Pattern Recognition*, 2024, pp. 5354–5363.
- [16] X. Lyu, Y.-T. Sun, Y.-H. Huang, X. Wu, Z. Yang, Y. Chen, J. Pang, and X. Qi, "3dgsr: Implicit surface reconstruction with 3d gaussian splatting," *ACM Transactions on Graphics (TOG)*, vol. 43, no. 6, pp. 1–12, 2024.
- [17] M. Yu, T. Lu, L. Xu, L. Jiang, Y. Xiangli, and B. Dai, "Gsd: 3dgs meets sdf for improved neural rendering and reconstruction," *Advances in Neural Information Processing Systems*, vol. 37, pp. 129 507–129 530, 2024.
- [18] B. Mildenhall, P. P. Srinivasan, M. Tancik, J. T. Barron, R. Ramamoorthi, and R. Ng, "Nerf: Representing scenes as neural radiance fields for view synthesis," *Communications of the ACM*, vol. 65, no. 1, pp. 99–106, 2021.
- [19] P. Wang, L. Liu, Y. Liu, C. Theobalt, T. Komura, and W. Wang, "Neus: Learning neural implicit surfaces by volume rendering for multi-view reconstruction," *arXiv preprint arXiv:2106.10689*, 2021.
- [20] L. Yariv, J. Gu, Y. Kasten, and Y. Lipman, "Volume rendering of neural implicit surfaces," *Advances in Neural Information Processing Systems*, vol. 34, pp. 4805–4815, 2021.
- [21] X. Zhang, R. Yu, and S. Ren, "Neural implicit representations for multi-view surface reconstruction: A survey," *IEEE Transactions on Visualization and Computer Graphics*, 2025.
- [22] M. Oechsle, S. Peng, and A. Geiger, "Unisurf: Unifying neural implicit surfaces and radiance fields for multi-view reconstruction," in *Proceedings of the IEEE/CVF international conference on computer vision*, 2021, pp. 5589–5599.
- [23] Z. Yu, S. Peng, M. Niemeyer, T. Sattler, and A. Geiger, "Monosdf: Exploring monocular geometric cues for neural implicit surface reconstruction," *Advances in neural information processing systems*, vol. 35, pp. 25 018–25 032, 2022.
- [24] Q. Fu, Q. Xu, Y. S. Ong, and W. Tao, "Geo-neus: Geometry-consistent neural implicit surfaces learning for multi-view reconstruction," *Advances in Neural Information Processing Systems*, vol. 35, pp. 3403–3416, 2022.
- [25] H. Li, X. Yang, H. Zhai, Y. Liu, H. Bao, and G. Zhang, "Voxsurf: Voxel-based implicit surface representation," *IEEE Transactions on Visualization and Computer Graphics*, vol. 30, no. 3, pp. 1743–1755, 2022.
- [26] L. Wang, Y.-T. Liu, J. Yang, W. Chen, X. Meng, B. Yang, J. Li, and L. Gao, "Hsdf: Hybrid sign and distance field for neural representation of surfaces with arbitrary topologies," *IEEE Transactions on Visualization and Computer Graphics*, vol. 31, no. 9, pp. 5215–5228, 2024.
- [27] S. Ye, Y. Hu, M. Lin, Y.-H. Wen, W. Zhao, Y.-J. Liu, and W. Wang, "Indoor scene reconstruction with fine-grained details using hybrid representation and normal prior enhancement," *IEEE Transactions on Visualization and Computer Graphics*, 2024.
- [28] B. Wang, Z. Yu, B. Yang, J. Qin, T. Breckon, L. Shao, N. Trigoni, and A. Markham, "Rangeudf: Semantic surface reconstruction from 3d point clouds," *arXiv preprint arXiv:2204.09138*, 2022.
- [29] C. Zhang, W. Su, Q. Xu, X. Liao, and W. Tao, "Pg-neus: Robust and efficient point guidance for multi-view neural surface reconstruction," *IEEE Transactions on Visualization and Computer Graphics*, 2024.
- [30] X.-K. Xiang, Y.-J. Yuan, W.-B. Hu, Y.-T. Liu, Y.-W. Ma, and L. Gao, "Pgt-neus: Progressive-growing tri-plane representation for neural surface reconstruction," *IEEE Transactions on Visualization and Computer Graphics*, 2025.
- [31] W. Su, C. Zhang, Q. Xu, and W. Tao, "Psd: Prior-driven neural implicit surface learning for multi-view reconstruction," *IEEE Transactions on Visualization and Computer Graphics*, 2024.
- [32] L. Yang, B. Deng, and J. Zhang, "Scalable and high-quality neural implicit representation for 3d reconstruction," *IEEE Transactions on Visualization and Computer Graphics*, 2025.
- [33] B. Wang, L. Chen, and B. Yang, "Dm-nerf: 3d scene geometry decomposition and manipulation from 2d images," *arXiv preprint arXiv:2208.07227*, 2022.
- [34] T. Müller, A. Evans, C. Schied, and A. Keller, "Instant neural graphics primitives with a multiresolution hash encoding," *ACM transactions on graphics (TOG)*, vol. 41, no. 4, pp. 1–15, 2022.
- [35] Z. Li, T. Müller, A. Evans, R. H. Taylor, M. Unberath, M.-Y. Liu, and C.-H. Lin, "Neuralangelo: High-fidelity neural surface reconstruction," in *Proceedings of the IEEE/CVF Conference on Computer Vision and Pattern Recognition*, 2023, pp. 8456–8465.
- [36] X. Liu, Q. Zhang, X. Huang, Y. Feng, G. Zhou, and Q. Wang, "H_{2}o-nerf: Radiance fields reconstruction for two-hand-held objects," *IEEE Transactions on Visualization and Computer Graphics*, 2025.
- [37] L. Yariv, P. Hedman, C. Reiser, D. Verbin, P. P. Srinivasan, R. Szeliski, J. T. Barron, and B. Mildenhall, "Baked sdf: Meshing neural sdf for real-time view synthesis," in *ACM SIGGRAPH 2023 Conference Proceedings*, 2023, pp. 1–9.
- [38] M.-J. Rakotosaona, F. Manhardt, D. M. Arroyo, M. Niemeyer, A. Kundu, and F. Tombari, "Nerfmeshing: Distilling neural radiance fields into geometrically-accurate 3d meshes," in *2024 international conference on 3D vision (3DV)*. IEEE, 2024, pp. 1156–1165.
- [39] E. Ramon, G. Triginer, J. Escur, A. Pumarola, J. Garcia, X. Giró-i Nieto, and F. Moreno-Noguer, "H3d-net: Few-shot high-fidelity 3d head reconstruction," in *Proceedings of the IEEE/CVF International Conference on Computer Vision*, 2021, pp. 5620–5629.
- [40] T. Lu, M. Yu, L. Xu, Y. Xiangli, L. Wang, D. Lin, and B. Dai, "Scaffold-gs: Structured 3d gaussians for view-adaptive rendering," in *Proceedings of the IEEE/CVF Conference on Computer Vision and Pattern Recognition*, 2024, pp. 20 654–20 664.
- [41] G. Fang and B. Wang, "Mini-splatting: Representing scenes with a constrained number of gaussians," in *European Conference on Computer Vision*. Springer, 2024, pp. 165–181.
- [42] —, "Mini-splatting2: Building 360 scenes within minutes via aggressive gaussian densification," *arXiv preprint arXiv:2411.12788*, 2024.
- [43] H. Chen, C. Li, and G. H. Lee, "Neusg: Neural implicit surface reconstruction with 3d gaussian splatting guidance," *arXiv preprint arXiv:2312.00846*, 2023.
- [44] D. Li, S.-S. Huang, and H. Huang, "Mpgs: Multi-plane gaussian splatting for compact scenes rendering," *IEEE Transactions on Visualization and Computer Graphics*, 2025.
- [45] Z. Bao, G. Liao, K. Zhou, K. Liu, Q. Li, and G. Qiu, "Loopsparsesg: Loop based sparse-view friendly gaussian splatting," *IEEE Transactions on Image Processing*, 2025.
- [46] R. Fan, J. Wu, X. Shi, L. Zhao, Q. Ma, and L. Wang, "Fov-gs: Foveated 3d gaussian splatting for dynamic scenes," *IEEE Transactions on Visualization and Computer Graphics*, 2025.
- [47] Z. Fan, S.-S. Huang, Y. Zhang, D. Shang, J. Zhang, Y. Guo, and H. Huang, "Rgavatar: Relightable 4d gaussian avatar from monocular videos," *IEEE Transactions on Visualization and Computer Graphics*, 2025.
- [48] Y. Wang, X. Wei, M. Lu, and G. Kang, "Plgs: Robust panoptic lifting with 3d gaussian splatting," *IEEE Transactions on Image Processing*, 2025.
- [49] Y. Wang, J. Wang, R. Gao, Y. Qu, W. Duan, S. Yang, and Y. Qi, "Look at the sky: Sky-aware efficient 3d gaussian splatting in the wild," *IEEE Transactions on Visualization and Computer Graphics*, 2025.
- [50] K. Tang, S. Yao, and C. Wang, "ivr-gs: Inverse volume rendering for explorable visualization via editable 3d gaussian splatting," *IEEE Transactions on Visualization and Computer Graphics*, 2025.
- [51] X. Tong, T. Shao, Y. Weng, Y. Yang, and K. Zhou, "As-rigid-as-possible deformation of gaussian radiance fields," *IEEE Transactions on Visualization and Computer Graphics*, 2025.
- [52] Y. Shi, D. Rong, B. Ni, C. Chen, and W. Zhang, "Garf: Geometry-aware generalized neural radiance field," *arXiv preprint arXiv:2212.02280*, 2022.
- [53] K. Ren, L. Jiang, T. Lu, M. Yu, L. Xu, Z. Ni, and B. Dai, "Octree-gs: Towards consistent real-time rendering with lod-structured 3d gaussians," *arXiv preprint arXiv:2403.17898*, 2024.
- [54] J. T. Barron, B. Mildenhall, D. Verbin, P. P. Srinivasan, and P. Hedman, "Mip-nerf 360: Unbounded anti-aliased neural radiance fields," in *Proceedings of the IEEE/CVF conference on computer vision and pattern recognition*, 2022, pp. 5470–5479.
- [55] A. Knapitsch, J. Park, Q.-Y. Zhou, and V. Koltun, "Tanks and temples: Benchmarking large-scale scene reconstruction," *ACM Transactions on Graphics*, vol. 36, no. 4, 2017.
- [56] A. Gropp, L. Yariv, N. Haim, M. Atzmon, and Y. Lipman, "Implicit geometric regularization for learning shapes," *arXiv preprint arXiv:2002.10099*, 2020.
- [57] H. Aanæs, R. R. Jensen, G. Vogiatzis, E. Tola, and A. B. Dahl, "Large-scale data for multiple-view stereo," *International Journal of Computer Vision*, vol. 120, pp. 153–168, 2016.
- [58] P. Hedman, J. Philip, T. Price, J.-M. Frahm, G. Drettakis, and G. Brostow, "Deep blending for free-viewpoint image-based rendering," *ACM Transactions on Graphics (ToG)*, vol. 37, no. 6, pp. 1–15, 2018.